Check for updates

JGR Planets

RESEARCH ARTICLE
10.1029/2025JE009028

Conjugated Silicate Nanodroplets in Lunar Regolith: Unraveling Impact-Driven Phase Separation

Yiheng Dai[1,2], Zhiheng Xie[1,2], Zezhou Li[1,2], Tianyi Jia[2,3], Ruimin Wang[2,3], Zongjun Yin[4], Bing Shen[2,3], and Jihan Zhou[1,2]

[1]Beijing National Laboratory for Molecular Sciences, Center for Integrated Spectroscopy, College of Chemistry and Molecular Engineering, Peking University, Beijing, China, [2]Research Institute of Extraterrestrial Material at Peking University (RIEMPKU), Beijing, China, [3]Ministry of Education Key Laboratory of Orogenic Belts and Crustal Evolution, School of Earth and Space Sciences, Peking University, Beijing, China, [4]State Key Laboratory of Palaeobiology and Stratigraphy, Nanjing Institute of Geology and Palaeontology, Chinese Academy of Sciences, Nanjing, China

Abstract Meteoroid impacts, a key process of space weathering, significantly alter the structures, compositions and properties of lunar regolith. However, the phase separation phenomena, common in lunar regolith and induced by impact, remain poorly understood. This uncertainty arises from the structural complexity and the scarcity of identified impact-induced phase separation features. Here we report the impact-induced formation of chemically distinct amorphous silicate nanodroplets, including iron-rich droplets within a silicon-rich glass matrix and vice versa, on the surface of a Chang'e-5 lunar regolith grain. These nanodroplets are partially ripened aggregates, and their formation is attributed to metastable liquid immiscibility driven by local chemical heterogeneities and rapid quenching. Additionally, troilite-kamacite remnants and skeletal crystallites of ilmenite and apatite provide direct evidence of impact and fast post-impact quenching, respectively. These findings suggest that quenched impact melts in airless bodies can undergo unmixing, forming immiscible conjugated nanodroplets, and exhibiting diverse behaviors under specific post-impact conditions.

Plain Language Summary The Moon's surface layer is continually modified by the impacts of meteoroids and micrometeoroids, altering its chemical composition and leading to the formation of characteristic structures. The behaviors of impact melts are not clearly resolved. Here we report on the chemically conjugated silicate nanodroplets discovered in the surface region of a Chang'e-5 lunar regolith grain. Remains of meteoroids and tiny mineral crystals are also found near these nanodroplets. These nanodroplets are clusters with unordered atomic arrangements, indicating the quick decrease in temperature. Based on their chemical compositions, we attribute their formation to the local variations in chemical makeup and rapid quenching after the impact event.

Key Points:

- Chemically conjugated silicate nanodroplets and meteoroid remnants were discovered in a Chang'e-5 lunar regolith grain
- The silicate nanodroplets are amorphous and form partially ripened aggregates
- The formation of nanodroplets is attributed to silicate liquid immiscibility driven by chemical heterogeneities and rapid quenching

Supporting Information:

Supporting Information may be found in the online version of this article.

Correspondence to:

Z. Yin, B. Shen and J. Zhou,
zjyin@nigpas.ac.cn;
bingshen@pku.edu.cn;
jhzhou@pku.edu.cn

Citation:

Dai, Y., Xie, Z., Li, Z., Jia, T., Wang, R., Yin, Z., et al. (2025). Conjugated silicate nanodroplets in lunar regolith: Unraveling impact-driven phase separation. *Journal of Geophysical Research: Planets*, *130*, e2025JE009028. https://doi.org/10.1029/2025JE009028

Received 27 FEB 2025
Accepted 23 MAY 2025

Author Contributions:

Conceptualization: Zongjun Yin, Bing Shen, Jihan Zhou
Data curation: Yiheng Dai
Formal analysis: Yiheng Dai, Zhiheng Xie
Funding acquisition: Zongjun Yin, Bing Shen, Jihan Zhou
Investigation: Yiheng Dai, Zhiheng Xie, Zezhou Li, Tianyi Jia, Ruimin Wang, Zongjun Yin, Bing Shen
Methodology: Jihan Zhou
Project administration: Jihan Zhou
Resources: Jihan Zhou
Supervision: Jihan Zhou
Validation: Yiheng Dai
Visualization: Yiheng Dai
Writing – original draft: Yiheng Dai, Jihan Zhou
Writing – review & editing: Yiheng Dai, Zhiheng Xie, Zongjun Yin, Bing Shen, Jihan Zhou

© 2025. American Geophysical Union. All Rights Reserved.

1. Introduction

Space weathering incessantly modifies airless bodies such as the Moon (Bennett et al., 2013; Pieters & Noble, 2016), altering the structure, chemical composition and physical properties of the surface regolith. The harsh space environment including solar wind ions, high-energy cosmic rays and hypervelocity impactors leads to distinctive surface regolith features such as amorphous rims (Christoffersen et al., 1996; L. P. Keller & McKay, 1993, 1997) or Fe^0 nanoparticles (Cymes et al., 2022; C. Li et al., 2022; Xian et al., 2023), and makes spectral changes (Blewett et al., 2021; Cassidy & Hapke, 1975) in extraterrestrial materials. Meteoroids and comets can transport interplanetary substances such as organic carbon and ferrous materials such as troilite or Fe–Ni alloys across the solar system. It has been estimated that the surface soil of the Moon and Mercury contains ∼1%–4% and ∼5%–20% meteoritic components, respectively (Noble et al., 2007). Meteoroids also play an important role in the gardening of surface materials on airless bodies and in the formation of breccia rocks. The average impact velocity on the Moon is calculated to be ∼13 $km{\cdot}s^{-1}$, with the maximum velocity potentially exceeding 50 $km{\cdot}s^{-1}$ (Cintala, 1992). The impact mass flux of $\sim 1.9 \times 10^{-16}$ $g{\cdot}cm^{-2}$ s^{-1} on the Moon allows sufficient input of materials and energy to modify the lunar surface (Bruno et al., 2007). As a result, the Moon is covered by a surface regolith layer of several meters thick, with an overturning rate estimated at 1 $m{\cdot}Gyr^{-1}$ (Heiken et al., 1991). Moreover, the absence of air and water on the Moon surface permits for the preservation of structures induced by space weathering, such as impact glass, agglutinates and novel minerals formed by impact-

induced shocking, melting and vaporization. These features are well-preserved in the upmost layer of lunar soil grains (J. Yang & Du, 2024; Zellner, 2019), offering insights into the principles of mass-energy interactions in space weathering.

Energy released by impactors can melt both lunar rock/soil and the impactors, generating melt with mixed composition. The subsequent cooling of melt would cause crystallization of minerals, glass formation due to quenching, or some unique structures caused by silicate liquid immiscibility (SLI). SLI has been observed in some terrestrial (Charlier et al., 2013; Sensarma & Palme, 2013) and Apollo lunar (Roedder & Weiblen, 1970, 1971) rocks, serving as an explanation for the chemical unmixing phenomena of anhydrous silicate melts during magma evolution. Briefly, when post-cooling below the upper consolute temperature, it is widely accepted that the mono-phase silicate melt with the composition falling into the miscibility gap will separate into two distinct phases with sharp interface: basaltic Fe-rich melt and felsic K-Si-rich melt (Thompson et al., 2007). Besides magma evolution, meteoroid impacts can also provide conditions such as sufficient heat for melting, intimate mixing of original lithologies and sufficiently rapid quenching rate to generate characteristic glassy silicate emulsions in impact melt rocks or impact glasses (Hamann et al., 2018). As for lunar regolith samples, detailed analysis of SLI structures on the grain surface at the submicron and nano scales will shed light on deeper understandings of space weathering mechanisms on airless bodies and the immiscibility process under impact conditions.

On 17 December 2020, the Chang'e-5 (CE-5) mission successfully returned 1,731 g of lunar soil samples from the Northern Oceanus Procellarum (43.06°N, 51.92°W) (Chen et al., 2023; C. L. Li et al., 2022; Wu et al., 2024). Previous studies on CE-5 regolith samples suggest that meteoroid impacts account for a significant proportion in the space weathering modification process affecting CE-5 samples, generating Fe^0 nanoparticles and impact glass particles with unique morphologies (C. Li et al., 2022; Zhao et al., 2023). Thus, the CE-5 regolith samples offer a unique opportunity to study the space weathering behaviors under impact conditions, especially the physio-chemical evolution mechanisms of shocked materials at nanometer and atomic scales, including material mixing, phase separation, and element redistribution.

In this study, we identified a modified region on a CE-5 regolith grain, which we attribute to an impact event. The region of interest is surrounded by smooth depressions of degassing pits and contains partially decomposed troilite fragments with small spherical remnants. We discovered five conjugated phase pairs related to SLI accompanied by crystallites of apatite and ilmenite. Among these conjugated phase pairs, we observed amorphous Fe-rich nanodroplets, ranging from ∼5 to ∼80 nm, embedded in K-Si-rich glassy matrix, and two types of silicate emulsion comprising Si-rich nanodroplets (∼50 nm in diameter) within an Fe-rich matrix. Detailed structural and chemical analyses of these textures suggest that the evolutionary process of lunar soil under impact conditions may involve local compositional heterogeneity and rapid quenching of impact melts.

2. Materials and Methods

2.1. Sample Preparation of Chang'e-5 Lunar Regolith Sample

The Chang'e-5 lunar regolith samples were shoveled from the lunar surface by the Chang'e-5 lander. We acquired 500 mg of Chang'e-5 samples (CE5C0600) allocated by the China National Space Administration. The sample was sieved by a 100-mesh sieve to keep grains larger than 100 μm, and the grains were dispersed on a conductive carbon tape sticking to a scanning electron microscope (SEM) sample stub made of aluminum. The samples were coated with Pt (∼30 nm thick) to enhance the conductivity. SEM images were acquired at 15 kV by a ThermoFisher Quattro environmental scanning electron microscope (ESEM) at the Electron Microscopy Laboratory of Peking University.

The preparation of three ultra-thin focused ion beam (FIB) slices was performed by a Zeiss Crossbeam 550 dual-beam focused ion beam scanning electron microscope (FIB-SEM) at Nanjing Institute of Geology and Palaeontology, Chinese Academy of Sciences. A protection layer of carbon and Pt was deposited on the regions of interest to prevent damage from Ga^+ ions. Milling of FIB slices was operated at a high voltage of 30 kV and the beam currents of 1–3 nA. The slices were then polished at 5 and 15 kV with the beam currents of 50–500 pA. All the samples and FIB slices were preserved in an argon-filled glove box to prevent any oxidation and contamination.

21699100, 2025, 7, Downloaded from https://agupubs.onlinelibrary.wiley.com/doi/10.1029/2025JE009028 by Sergio Sancevero - Capes , Wiley Online Library on [06/06/2026]. See the Terms and Conditions (https://onlinelibrary.wiley.com/terms-and-conditions) on Wiley Online Library for rules of use; OA articles are governed by the applicable Creative Commons License

21699100, 2025, 7, Downloaded from https://agupubs.onlinelibrary.wiley.com/doi/10.1029/2025JE009028 by Sergio Sancevero - Capes , Wiley Online Library on [06/06/2026]. See the Terms and Conditions (https://onlinelibrary.wiley.com/terms-and-conditions) on Wiley Online Library for rules of use; OA articles are governed by the applicable Creative Commons License

2.2. TEM, STEM and EDS Experiments

For transmission electron microscopy (TEM), scanning transmission electron microscopy (STEM) and energy-dispersive X-ray spectroscopy (EDS) experiments, a ThermoFisher Titan Themis Z microscope equipped with a high-angle annular dark field (HAADF) detector and four windowless silicon drift EDS detectors (ThermoFisher Super-X, with a solid angle of 0.7 srad and 120 mm^2 combined detector area) at the Analytical Instrument Center of Peking University was used. All the TEM, STEM and EDS data were collected at 300 kV with an electron beam current of ∼200 pA for EDS mappings and ∼30 pA for HAADF-STEM imaging. The convergence semi-angle was 25 mrad when collecting HAADF-STEM images.

The EDS data were collected as the measurement of emitted X-rays from regions probed by the electron beam, and the typical total electron dose of an EDS map was 5,000–15,000 $e^{-}\cdot Å^{-2}$. No sample damage was visible at such electron doses. During the EDS data collection, the images were drift-corrected over the whole procedure. For the analysis of EDS data, the background was subtracted in all the spectra to get the net intensities of X-rays, and the K lines of every element were fitted by Gaussian models using the ThermoFisher Velox software. Then, Cliff-Lorimer factors ("K-factors") calculated at 300 kV were used in Velox to convert the intensities of X-rays into the quantitative elemental compositions.

3. Results

3.1. Impact-Related Textures on the Surface of the Researched Grain

The target of this study was a lunar soil grain from CE-5 samples with distinct impact-induced surface features ("Materials and Methods", Figure 1a). Based on EDS measurements, this grain has a Fe-rich composition (FeO = ∼20 wt%, MgO = ∼5 wt%, CaO = ∼12 wt%, Al_2O_3 = ∼16 wt% and TiO_2 = ∼5 wt%) and consists of several types of minerals and glasses with different elemental compositions (Table S1 in Supporting Information S1). Several smooth depressions with diameters of ∼5–25 μm were detected on the surface of the grain (Figure 1a), and various impact-related features were also discovered, including melting glass with smooth surface and voids, adhered particles and glassy beads. We focused on a space-weathered area with unique surface morphologies (Figure 1b and Figure S2 in Supporting Information S1) near the depressions. EDS mapping confirms that this area mainly consists of ilmenite (il) surrounded by anorthite substrate, as well as some regions rich in sulfur and phosphorus (Figure S1 in Supporting Information S1). The ilmenite crystallites embedded in the silicate glass exhibit distinct skeletal structure. The ilmenite grains, ranging from 100 to 300 nm, are composed of aggregations with sizes of 10–50 nm (Figure 1c and Figure S2 in Supporting Information S1).

To explore the internal structures, three slices (Slice-1, Slice-2 and Slice-3) were cut out from this grain using FIB technique in a dual beam system ("Materials and Methods"). Slice-1 was cut from a region rich in sulfur and phosphorus, exhibiting multiple phases (Figure 1d and Figure S3a in Supporting Information S1), including mineral crystals of apatite (Apt) and anorthite, silicate glass, Si-rich nanodroplets within silicate emulsion regions and meteoroid remnants such as kamacite (Ka) and troilite (Tro). Plenty of crystal defects were found in the apatite crystals (Figures S4b and S4c in Supporting Information S1). The anorthite crystal at the top of the slice features a 150-nm-thick solar wind-damaged rim and solar energetic particle tracks inside the crystal with a density of $\sim 1.1 \times 10^{11}$ $Tracks\cdot cm^{-2}$ (Figures S4d–S4f in Supporting Information S1). This finding implies an exposure history of ∼2.5 million years after this grain was overturned to the lunar surface (Lindsay P. Keller et al., 2021).

The remaining two slices were prepared from the central (Slice-2) and peripheral regions (Slice-3) of the ilmenite, respectively (Figure 1b). Slice-2 contains smooth and connected ilmenite crystallites (which is the cross-sectional view of the skeletal ilmenites) with silicate glasses filling the interstitial space (Figure 1e and Figure S3b in Supporting Information S1). Slice-3, similar in composition to Slice-2, displays dendritic crystallites of ilmenite embedded within the layers of heterogeneous glasses (Figure 1f and Figure S3c in Supporting Information S1). Si-rich nanodroplets are also observed in the silicate emulsion regions of this slice, akin to those found in Slice-1. Unique Fe-rich silicate nanodroplets are found at the interfaces between heterogeneous glass phases in all the three slices, especially in Slice-3 where a layer of nanodroplets intersects across the matrix (Figure 1f).

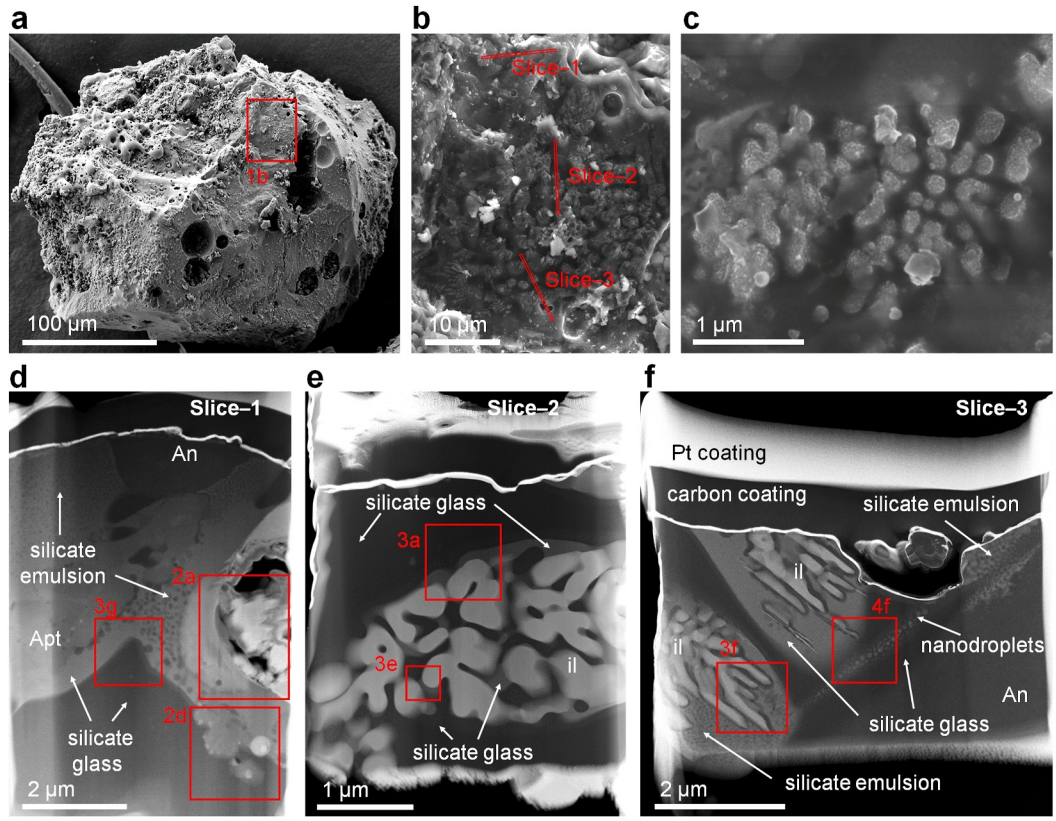

Figure 1. Grain surface features and structures. (a) Secondary electron (SE) image of the whole view of the target CE-5 grain. (b) SE image of the area of interest containing space-weathered ilmenite (il) and anorthite (An) substrate with the position of focused ion beam (FIB) slices marked by red rectangles. (c) Enlarged SE image of the skeletal ilmenite crystallites embedded in the silicate matrix. Note that the contrast of siliceous matrix is relatively low compared with the ilmenite crystallites, and the top surface of this region is flat (Figures S2e and S2f in Supporting Information S1). (d) High-angle annular dark field (HAADF) image of FIB Slice-1 shows the multi-phase textures, including silicate emulsions, silicate glass, impactor residues and crystals of apatite (Apt) and anorthite. (e) HAADF images of FIB Slice-2 prepared at the center of space-weathered ilmenite region, containing ilmenite crystallites with skeletal texture surrounded by silicate glass. (f) HAADF image of FIB Slice-3 prepared at the edge of skeletal ilmenite region, consisting of ilmenite crystallites, silicate glass, Si-rich nanodroplets in silicate emulsion regions, a layer of secondary Fe-rich nanodroplets and anorthite substrate.

3.2. Troilite and Kamacite Fragments From Impactor Residues

Two distinct types of impactor residues were identified in Slice-1. The first type consists of irregular fragments surrounded by voids (Figure 2a). The fragments are mostly kamacite consisting of almost pure iron with extremely low amounts of Ni (lower than the detection limit of EDS). A piece of troilite was observed in the bottom of the fragments (Figure 2b). HAADF image at atomic resolution further confirms that the iron atoms in kamacite are arranged in a body-centered cubic (bcc) lattice (Figure 2c). The other type of impactor residue comprises spherical fragments with diameters ranging from 50 to 350 nm (Figure 2d). These spherical fragments are distributed in the whole FIB slice. Most of them are imperfect spheres with small vesicles, which may be attributed to the vaporizing of sulfur due to the impact (orange arrows in Figure 2d). Selected area electron diffraction (SAED) (Figure S5 in Supporting Information S1) and EDS mapping (Figure 2e) show that these fragments are mainly troilites, within which very low Ni content was found (<0.1 wt%, Figure S6 in Supporting Information S1). There are kamacite granules with round edges distributed in a large spherical troilite (Figure 2d and Figure S5a in Supporting Information S1). HAADF images and EDS line profile results (Figure 2f) show the enrichment of Fe and decrease of S content at the Ka sites.

21699100, 2025, 7, Downloaded from https://agupubs.onlinelibrary.wiley.com/doi/10.1029/2025JE009028 by Sergio Sancevero - Capes , Wiley Online Library on [06/06/2026]. See the Terms and Conditions (https://onlinelibrary.wiley.com/terms-and-conditions) on Wiley Online Library for rules of use; OA articles are governed by the applicable Creative Commons License

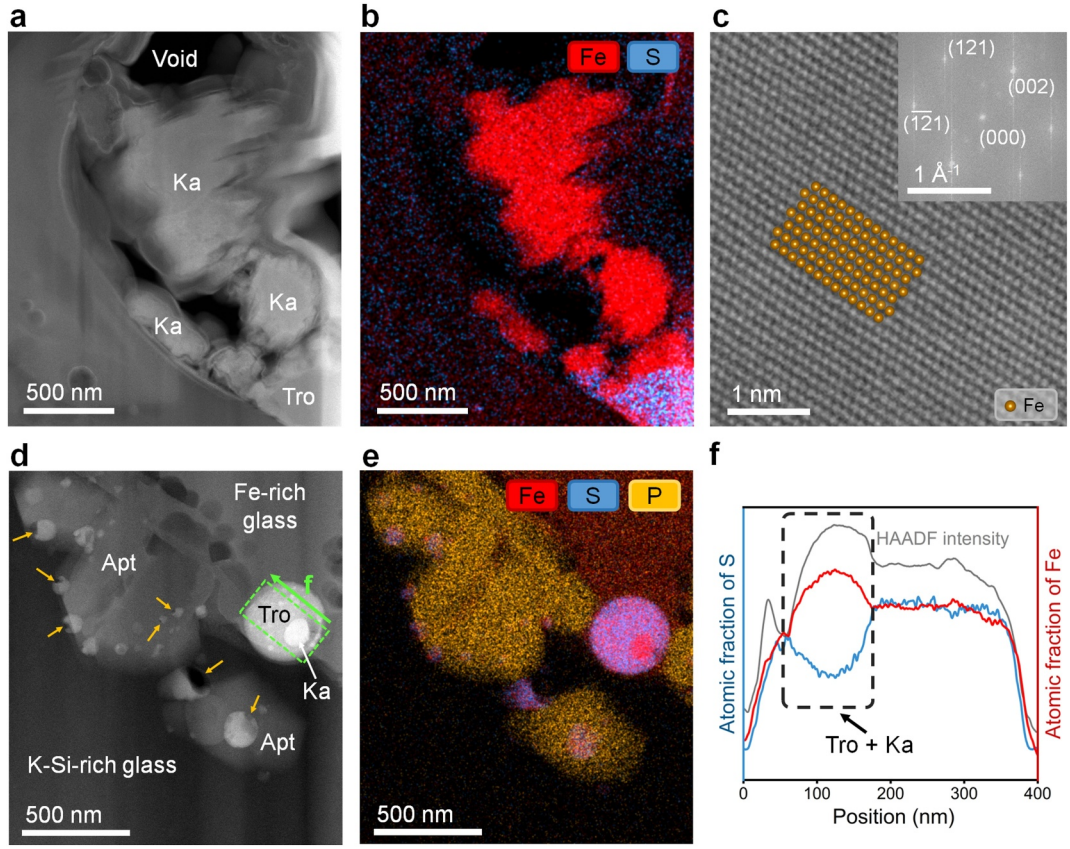

Figure 2. The composition and structure of meteoroid residue. (a–b) High-angle annular dark field (HAADF) image (a) and energy-dispersive X-ray spectroscopy (EDS) mapping (b) of irregular meteoroid fragments consisting of kamacite (Ka) and troilite (Tro). The Ka grains are covered by a layer of redeposited materials from FIB cutting. (c) HAADF image of Ka at atomic resolution. Ka exhibits a body-centered-cubic (bcc) structure. The insert image is the fast Fourier transform result showing the corresponding planes. (d–f) HAADF image (d), EDS mapping (e) and EDS line profiles (f) of circular Tro fragments embedded deeply in the glassy matrix materials. The positions of concaved vesicles next to the small troilite spherical fragments are marked by orange arrows. The Ka particle is marked by a black rectangle (f) where the HAADF intensity and atomic fraction of Fe increase while the atomic fraction of S decreases.

3.3. Heterogeneous Glassy Textures

The heterogeneous glassy textures consist of two major types of glassy mixtures with different morphologies and compositions. These glasses were found either near the impactor residues or next to the ilmenite crystallites.

One common type of glass mixture consists of continuous Fe-rich and Si-rich phases with the size of ~hundreds of nanometers. Two major Fe components were identified (Table S1 in Supporting Information S1), that is, Fe-Glass-1 (Figures 3a–3f) and Fe-Glass-2 (Figure 3g). Fe-Glass-1 is mainly composed of FeO (~44 wt%) and SiO_2 (~42 wt%) but much less TiO_2 (~1 wt%) and CaO (~5 wt%), while Fe-Glass-2 has less FeO (~28 wt%) and SiO_2 (~33 wt%) but higher TiO_2 (~11 wt%) and CaO (~12 wt%). Notable amount of P_2O_5 was found in Fe-Glass-2 (~7 wt%) while absent in Fe-Glass-1. The Si-rich phase, that is, K-Si-Glass, has extremely high SiO_2 (~86 wt%) and K_2O (~4 wt%) contents. HAADF imaging and EDS mapping reveal the sharp interfaces between ilmenite, Fe-Glass-1 and K-Si-Glass (Figures 3a and 3b). The interface between ilmenite and glass species is revealed by the HAADF image at the atomic level (Figure 3c and Figure S7f in Supporting Information S1), where Fe-Glass-1 exhibits fully disordered atomic features while the crystalline atomic columns of Fe and Ti in ilmenite are well distinguished, respectively. The Fe-rich silicate phases are amorphous glasses confirmed by the disordered atomic structures (Figure 3d) revealed by high resolution transmission electron microscopy and typical diffusive amorphous halo from SAED results (the inset of Figure 3d).

21699100, 2025, 7, Downloaded from https://agupubs.onlinelibrary.wiley.com/doi/10.1029/2025JE009028 by Sergio Sancevero - Capes , Wiley Online Library on [06/06/2026]. See the Terms and Conditions (https://onlinelibrary.wiley.com/terms-and-conditions) on Wiley Online Library for rules of use; OA articles are governed by the applicable Creative Commons License

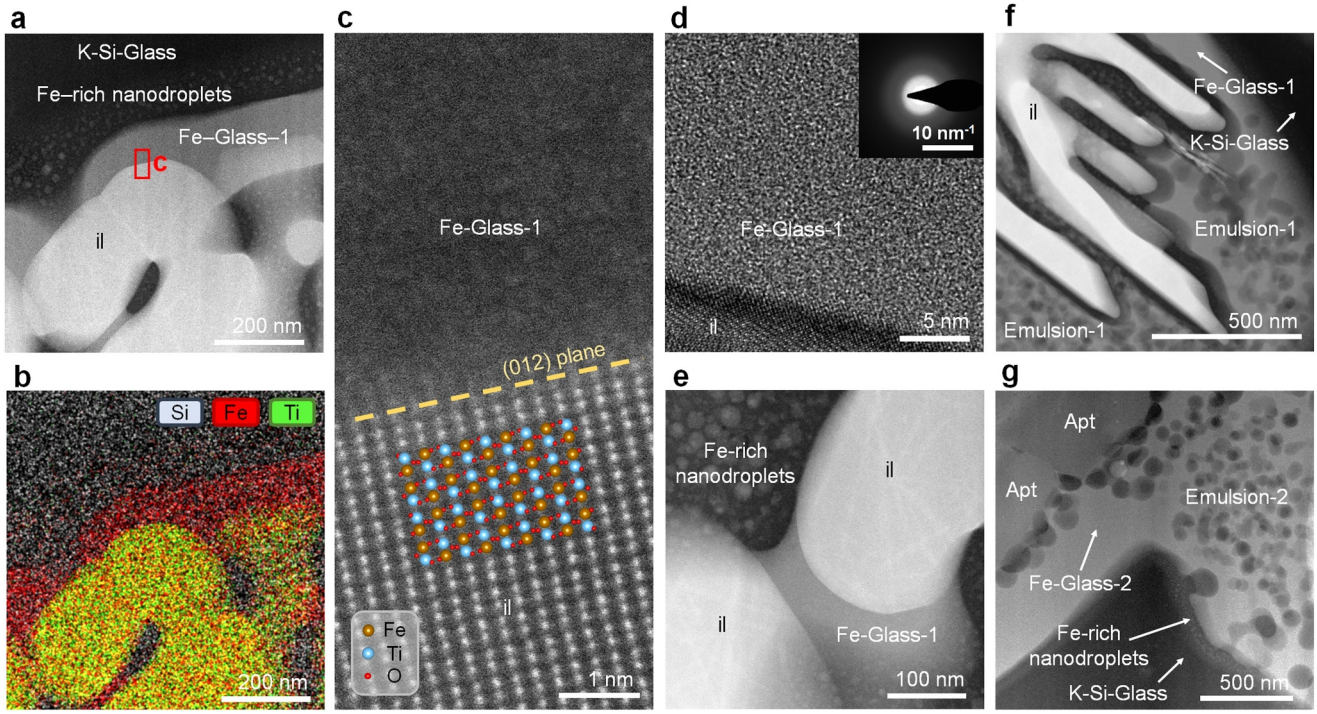

Figure 3. Structure of heterogeneous glass. (a–b) High-angle annular dark field (HAADF) image (a) and energy-dispersive X-ray spectroscopy mapping (b) of K-Si-rich silicate glass: K-Si-Glass and Fe-rich silicate glass: Fe-Glass-1 covering the ilmenite crystallites. Fe-rich nanodroplets are observed embedded in the K-Si-Glass matrix near the interface between Fe-rich and K-Si-rich phases. (c) HAADF image at atomic resolution shows the sharp interface between the ilmenite and Fe-Glass-1. The ilmenite crystallite image was acquired along the (12 $\bar{1}$) axis, and the interface is parallel to the (012) plane. (d) HRTEM and Selected area electron diffraction (insert) images of Fe-Glass-1 indicate its amorphous nature. (e) HAADF image of the coexisting ilmenite, Fe-Glass-1, K-Si-Glass and Fe-rich nanodroplets. (f) HAADF image of ilmenite crystallites in Slice-3 covered by silicate Emulsion-1, which is close to K-Si-Glass. The chemical compositions of Emulsion-1 in Slice-3 are FeO = ~35 wt%, CaO = ~4 wt%, TiO_2 = ~3 wt%, Al_2O_3 = ~11 wt% and SiO_2 = ~45 wt%. (g) HAADF image of silicate phase-separation structures in Slice-1, including Fe-rich silicate glass Fe-Glass-2, K-Si-Glass and silicate Emulsion-2. The chemical compositions of Emulsion-2 are FeO = ~23 wt%, CaO = ~11 wt%, TiO_2 = ~9 wt%, Al_2O_3 = ~8 wt%, P_2O_5 = ~6 wt% and SiO_2 = ~41 wt%. Some siliceous droplets are deformed when sticking to the apatite crystals.

The other type of glass mixture is silicate emulsions containing silicate nanodroplets, and can be divided into two subtypes.

3.3.1. Silicate Emulsions With Si-Rich Nanodroplets

The first subtype is silicate emulsions where Si-rich nanodroplets are embedded in Fe-rich silicate matrix (Figures 3f and 3g, Figures 4a–4c and Figures S7g–S7i in Supporting Information S1), and can be further divided into Emulsion-1 and Emulsion-2 based on the composition. These Si-rich nanodroplets interconnect and overlap, forming tube-like structures. Sharp meniscus interfaces were observed between two glass phases, and some Si-rich nanodroplets are deformed when sticking to the apatite crystals. Atomic resolution HAADF images confirm that these Si-rich nanodroplets and their Fe-rich matrix are both amorphous (Figure 4d). Statistically, the Si-rich nanodroplets have average diameters of 36 and 47 nm for Emulsion-1 and Emulsion-2 with broad size distribution (Figure 4e). The bulk compositions of these emulsions are slightly more siliceous than those of Fe-Glass-1 and Fe-Glass-2 (Table S1 in Supporting Information S1), while the compositions of Fe-rich silicate matrix of both emulsions are very similar to those of Fe-Glass-1 and Fe-Glass-2 respectively. From the result of EDS mapping, the enrichment of K is observable in Si-rich nanodroplets (Figure S8a in Supporting Information S1). Although the individual compositions of Si-rich nanodroplets are difficult to quantify directly from the EDS maps due to their overlapping with the Fe-rich substrate, we estimated their compositions by mathematical fitting based on several assumptions (see Table S1 in Supporting Information S1, for more calculation details).

21699100, 2025, 7, Downloaded from https://agupubs.onlinelibrary.wiley.com/doi/10.1029/2025JE009028 by Sergio Sancevero - Capes , Wiley Online Library on [06/06/2026]. See the Terms and Conditions (https://onlinelibrary.wiley.com/terms-and-conditions) on Wiley Online Library for rules of use; OA articles are governed by the applicable Creative Commons License

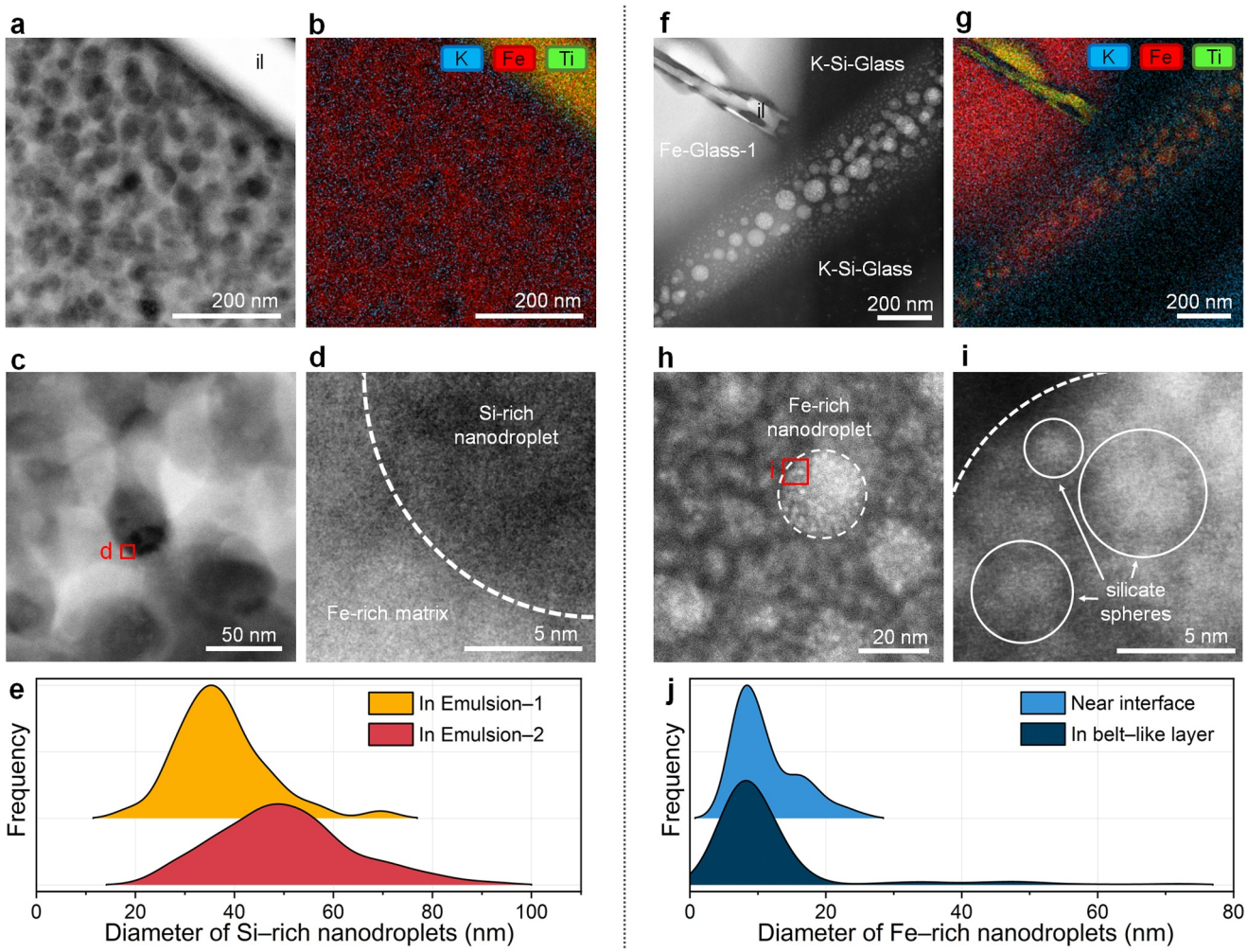

Figure 4. Chemical composition and structure of Fe-rich and Si-rich nanodroplets. (a–b) High-angle annular dark field (HAADF) image (a) and energy-dispersive X-ray spectroscopy (EDS) mapping (b) of Si-rich nanodroplets with enriched K element embedded in the silicate emulsion in Slice-3. (c–d) HAADF image of the emulsion (c) and enlarged HAADF image at the interface of one Si-rich nanodroplet and the Fe-rich matrix (d). Atomic resolution images show amorphous structures. (e) Size distributions of Si-rich nanodroplets. The average diameter of Si-rich nanodroplets is 36 nm in Emulsion-1 and 47 nm in Emulsion-2. (f–g) HAADF image (f) and EDS mapping (g) of Fe-rich nanodroplets gathering into a belt-like structure in Slice-3. Fe and Ti are enriched in these nanodroplets, while K is enriched in the matrix. (h–i) HAADF images of Fe-rich nanodroplets. These droplets are amorphous and composed of smaller clusters. The framboidal Fe-rich nanodroplet is marked by a dash circle, while the small spheres inside it are marked by solid circles. (j) Size distributions of Fe-rich nanodroplets. Most Fe-rich nanodroplets are 10-nm-sized, with a few larger ones having 15–80 nm in diameter.

3.3.2. Silicate Emulsions With Fe-Rich Nanodroplets

Fe-rich silicate nanodroplets embedded in the Si-rich substrate are widely observed (Figures 3a, 3e, 3g, and 4f and Figure S7a–S7e in Supporting Information S1) as the second subtype of silicate emulsions throughout this lunar grain. These Fe-rich nanodroplets have circular shapes and mainly can be found near the interface of Fe-Glass and K-Si-Glass. In Slice-3, abundant nanodroplets accumulated in a belt region with a total width of ∼300 nm (Figure 4f). The sizes of nanodroplets in the belt show an increase of ∼5 nm in periphery to ∼80 nm in the center. Compared with the Si-rich nanodroplets, the Fe-rich nanodroplets are much smaller and have narrower size distributions (Figure 4j). Framboidal Fe-rich nanodroplets were also discovered (the dash white circle in Figure 4h), and each sphere was less than 5 nm in size (Figure 4i). The atomic structures of these spheres (solid white circles in Figure 4i) are amorphous, indicating that they do not form any discernible crystal structures and remain as glasses within the siliceous matrix. The chemical compositions of the regions containing Fe-rich nanodroplets also show a typical zoning of Fe and K elements (Figure S8b in Supporting Information S1). Similar mathematical fitting methods were applied to determine the chemical composition of the nanodroplets

21699100, 2025, 7, Downloaded from https://agupubs.onlinelibrary.wiley.com/doi/10.1029/2025JE009028 by Sergio Sancevero - Capes , Wiley Online Library on [06/06/2026]. See the Terms and Conditions (https://onlinelibrary.wiley.com/terms-and-conditions) on Wiley Online Library for rules of use; OA articles are governed by the applicable Creative Commons License

and the matrix separately (see Supporting Information S1 for more details). The results indicate that the composition of Fe-rich nanodroplets (FeO = ~37 wt%, CaO = ~2 wt%, TiO_2 = ~13 wt%, Al_2O_3 = ~6 wt% and SiO_2 = ~38 wt%) are similar to those of Fe-Glass. In contrast, the glass matrix is highly Si-rich and similar to K-Si-Glass (SiO_2 = ~73 wt%, Al_2O_3 = ~11 wt% and K_2O = ~5 wt%) (Table S1 in Supporting Information S1).

4. Discussion

4.1. Impact-Induced Structures and Troilite Decomposition in the Lunar Regolith Grain

Microstructural and mineralogical analyses suggest that the studied grain (Figure 1b) likely originated from an impact event, as evidenced by meteoroid remnants and phase-separated structures featuring Fe-rich and Si-rich nanodroplets. The smooth depressions on the surface of this grain, characterized by sharp edges and absent uplifted rims (Figure 1a), resemble degassing pits, features typically associated with volatile release during impact heating (Rode et al., 1980; Yan et al., 2022) when implanted solar wind hydrogen and other volatiles are expelled, forming vesicles within the melt. Upon rapid quenching, these vesicles are trapped in the glassy matrix; subsequent impacts crack the glass, exposing the vesicles and creating degassing pits. Given the presence of an amorphous rim and solar energetic particle tracks in anorthite crystal (Figure S4 in Supporting Information S1), the impact event likely occurred no later than ~2 million years ago. This grain is hypothesized to be quenched ejecta from the impact, with its interior exposed to subsequent space weathering processes.

Troilite fragments in Slice-1 likely sourced from the impactor, given the immiscibility of sulfide and silicate melts, which results in spherical troilite fragments with sharp interfaces, a feature driven by high interfacial tension. This has been found in lunar basaltic samples (Heiken, 1975; L. Li et al., 2023; Yan et al., 2024) and chondrites (Rubin et al., 1999). The decomposition of troilite (Figures 2b and 2e) could be caused by the reducing effect of solar wind ions (Matsumoto et al., 2020) or thermal metamorphism with high temperature and low sulfur fugacity (fS_2) (Harries & Langenhorst, 2013). Given that the troilite remnants in this grain are far from the solar wind damage rim (Figure S4a in Supporting Information S1), the decomposition of troilite into kamacite should be attributed to the extremely low fS_2 in the lunar atmosphere and high post-shock temperature. fS_2 is estimated to be about −19 in log units based on dayside data (Stern, 1999), and a temperature above 650 K can trigger the decomposition of troilite into iron and sulfur (Toulmin & Barton, 1964). This accounts for the complete decomposition of troilite fragments exposed to the vacuum environment (Figures 2a and 2b) and partial decomposition of fragments deeply embedded in the glass matrix with some cavities close to the slightly deformed spherical troilite fragments (Figures 2d and 2e). The extremely low nickel contents of these kamacite and troilite fragments also agree with the assumption that these kamacite grains originated from troilite decomposition rather than from melt together with the troilite crystals.

4.2. Phase Separation in Melts and Nanosized Droplet Formation

Based on their morphology and composition, the previously observed heterogeneous glassy textures are interpreted as products of SLI. These textures include continuous unmixing glasses with Fe-rich and Si-rich phases (Fe-Glass-1, Fe-Glass-2 and K-Si-rich glass) adjacent to ilmenite crystallites, silica-rich nanodroplets embedded in Fe-rich silicate glassy matrix, and Fe-rich nanodroplets in Si-rich glassy matrix. To figure out the relationship among these different immiscible glasses, we illustrate their chemical compositions on a quasi-ternary phase diagram encompassing the components of CaO + MgO + FeO + TiO_2 + P_2O_5, Na_2O + K_2O + Al_2O_3 and SiO_2. The elements are divided as such because of the similar immiscibility fields in different ternary systems like CaO-Al_2O_3-SiO_2, MgO-Na_2O-SiO_2 etc., constituting a more general diagram than the leucite-fayalite-SiO_2 system (Roedder, 1978). The stable high-temperature miscibility gap, stable low-temperature miscibility gap and metastable immiscibility extent are marked in the phase diagram (Roedder, 1978; Visser & Koster Van Groos, 1979) (Figure 5a). The K-Si-Glass and Fe-Glass-1 are plotted on the metastable immiscibility extent, and their tie-lines are basically parallel to the extent of the stable two-liquid field (red dash lines in Figure 5a). Similar alignment is observed for the Fe-rich nanodroplets and their siliceous matrix (green dash line in Figure 5a). Notably, Fe-Glass-2 deviates from the metastable immiscibility extent, which could be attributed to the enlarging modification of the immiscibility gap by high amounts of TiO_2 and P_2O_5 (Freestone, 1978). As reported before, the existence of phosphorus could significantly modify the degree of polymerization of silicate melts at high temperature, adjusting the unmixing behaviors of melts (Mysen & Cody, 2001). We hypothesize that the precipitation of apatite and ilmenite crystals happened first, and then it could cause the compositional change of

21699100, 2025, 7, Downloaded from https://agupubs.onlinelibrary.wiley.com/doi/10.1029/2025JE009028 by Sergio Sancevero - Capes , Wiley Online Library on [06/06/2026]. See the Terms and Conditions (https://onlinelibrary.wiley.com/terms-and-conditions) on Wiley Online Library for rules of use; OA articles are governed by the applicable Creative Commons License

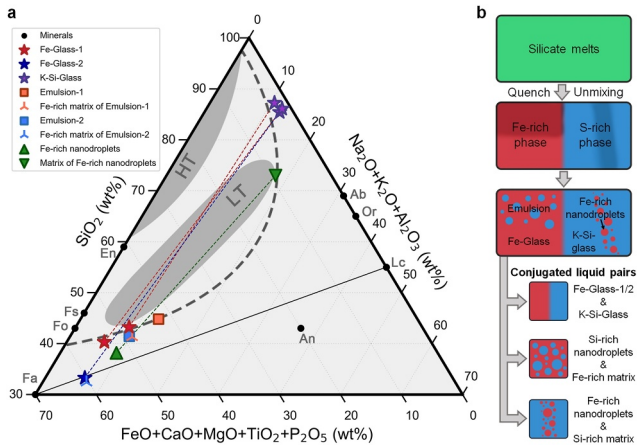

Figure 5. Phase analysis of phase-separated structures. (a) The quasi-ternary phase plot ($CaO + MgO + FeO + TiO_2 + P_2O_5$) – ($Na_2O + K_2O + Al_2O_3$) – SiO_2. The two stable miscibility gaps and metastable immiscible extent are shown by the gray areas and the bold dashed line, and the tie lines are presented as thin dashed lines. Minerals are also marked by dots at corresponding compositions. Abbreviations: Fa = Fayalite; Fo = Forsterite; Fs = Ferrosilite; En = Enstatite; Ab = Albite; Or = K-feldspar; Lc = Leucite; An = Anorthite. The Nernst partition coefficients of elements are listed in Table S2 in Supporting Information S1, with a similar trend from previous reports (Veksler et al., 2006). The compositions of Fe-Glasses (red and blue stars) and the matrix of silicate emulsions (trident star markers) are almost the same. The total compositions of silicate emulsions (square markers) are slightly deviated from Fe-Glasses. The fitted compositions of Si-rich nanodroplets in the silicate emulsions are shown in Figure S9 in Supporting Information S1, and the tie lines between the matrix and the Si-rich nanodroplets display similar trend with other phase-separated structures. (b) Illustration of the formation of conjugated liquid pairs including K-Si-rich Glass and Fe-Glasses, silicate emulsions containing Si-rich nanodroplets, and Fe-rich nanodroplets with their Si-rich matrix. The observed nanodroplets were formed due to the local compositional inhomogeneities in the primary unmixing Fe-rich and Si-rich phases.

initial melts, leaving a resultant melt whose composition fell in the metastable immiscibility gap, which triggered further phase separation. Otherwise, the compositions of Fe-rich and Si-rich glass would deviate from the immiscibility extent due to the precipitation of mineral crystals.

Although Fe-Glass-2 mostly connects to Emulsion-2 regions and locates next to K-Si-rich glass (Figure 3g), Si-rich nanodroplets are observed exclusively within Emulsion-2, and are absent in Fe-Glass-2. A similar phenomenon between Fe-Glass-1 and Emulsion-1 was also found. Our findings suggest that the Fe-Glasses and the initial melts of silicate emulsions may originate from the same unmixing process but with some subtle compositional variations. Thus, these initial melts of current silicate emulsions underwent further unmixing to form Si-rich nanodroplets. A comparable process may also happen in K-Si-Glass where the slightly heterogeneous distributions of Fe, Ti and Ca lead to the formation of Fe-rich nanodroplets. As a result, various conjugated melt pairs finally formed during the metastable unmixing process, including two pairs of K-Si-rich Glass and Fe-Glasses, two kinds of silicate emulsions containing Si-rich nanodroplets and Fe-rich matrix, and Fe-rich nanodroplets with their Si-rich matrix (Figure 5b).

Given that all the unmixing textures are amorphous glasses, and both Fe-rich and Si-rich nanodroplets embedded in the glass matrix range in sizes from 5 to ~80 nm, our observations suggest that after the impact, the high temperature melts experienced a quenching process with high cooling rates. This forced the liquids to solidify as various types of glasses (Hamann et al., 2018). The melts were in a nonequilibrium state and exhibited local heterogeneities in chemical composition (Y. Wu et al., 2023). The unmixing of different immiscible compositions occurred quickly, preventing the local inhomogeneous liquids from achieving equilibrium and thus facilitating the further unmixing and formation of nanodroplets (Figure 5b). Moreover, during the quenching process, the viscosity of the Si-rich liquid increased rapidly, becoming much higher than that of the Fe-rich phase (Thivet et al., 2023; Veksler et al., 2008). The increase of viscosity hindered the Ostwald ripening process of amorphous Fe-rich clusters in the Si-rich matrix, freezing these framboidal structures with relatively small sizes and preventing them from further aggregating. Conversely, larger Si-rich nanodroplets could form within the Fe-rich matrix, which has a lower viscosity accounting for better diffusion.

4.3. Implications for the Complex Phase-Separation Behaviors After Impact

We illustrate the space weathering process on this lunar soil grain based on our comprehensive analyses (Figure 6). Upon the initial impact, melts were ejected accompanied by the formation of degassing vesicles inside the melts. Troilite, likely as parts of the impactor, was mixed with the melted silicate substrate, subsequently crystalizing and decomposing to yield kamacite crystals alongside residual troilite. Following the impact, the ejected melt underwent rapid cooling followed by the formation of apatite and ilmenite crystallites. The remaining silicate melts then fell into the extent of metastable immiscibility gap. During quenching, the unmixing process happened in the melts, with the local inhomogeneous compositions leading to the formation of multiple pairs of conjugated silicate liquids, including continuous Fe-rich and Si-K-rich amorphous phases covering the previously precipitated crystallites, silicate emulsion of Fe-rich matrix with Si-rich nanodroplets, and glassy Fe-rich nanodroplets distributed in the Si-rich matrix. These textures were "frozen" in various glass species when the temperature dramatically dropped during quenching, thereby preserving a record of the complex phase separation process induced by impact.

Melt differentiation typically occurs via fractional crystallization, as evidenced in chondrites (Miyahara et al., 2008) and lunar rocks (Phinney et al., 1974). Our observations indicate that under specific temperature and composition conditions, the primary melt may undergo unmixing, forming immiscible conjugated liquid pairs

21699100, 2025, 7, Downloaded from https://agupubs.onlinelibrary.wiley.com/doi/10.1029/2025JE009028 by Sergio Sancevero - Capes , Wiley Online Library on [06/06/2026]. See the Terms and Conditions (https://onlinelibrary.wiley.com/terms-and-conditions) on Wiley Online Library for rules of use; OA articles are governed by the applicable Creative Commons License

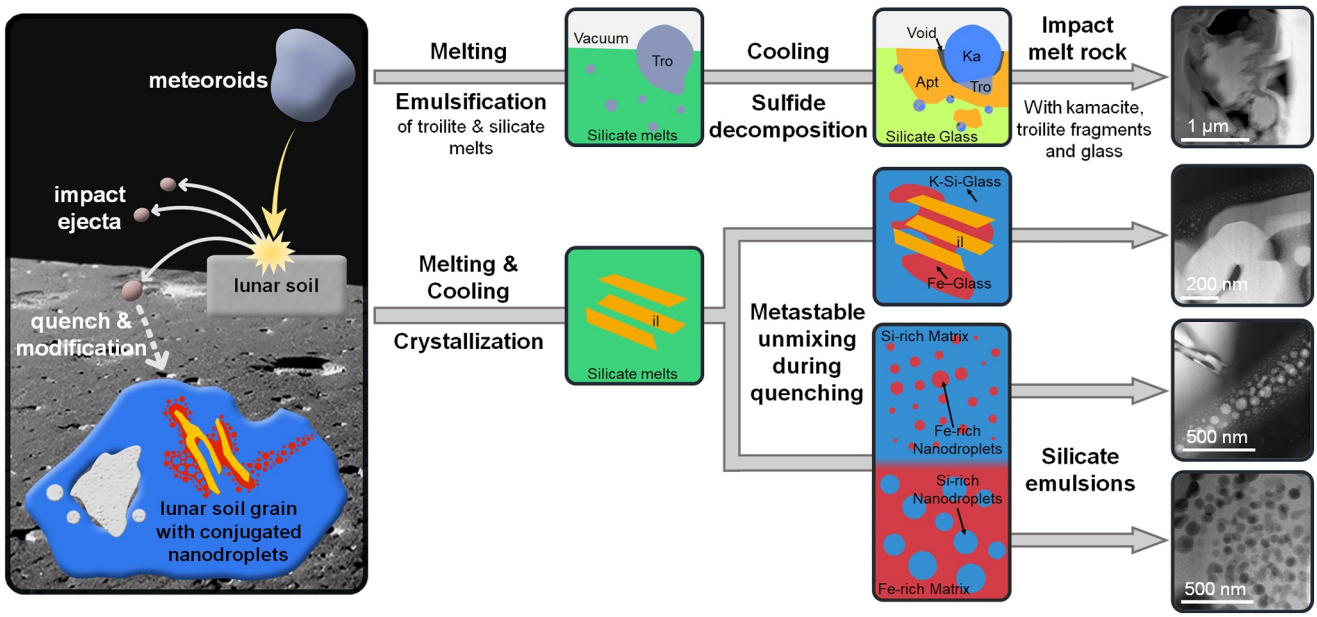

Figure 6. Formation mechanism of phase-separated structures containing nanosized droplets. Schematic illustration of the space-weathering process dominated by meteoroid impact causing the formation of phase-separated textures and nanometer-sized Fe-rich and Si-rich glassy droplets.

rather than precipitating mineral crystals. This occurs because the heat and pressure required for fractional crystallization are not sustained by impact energy. The high cooling rate of impact ejecta hinders nucleation and ripening due to the rapid increase in melt viscosity, preventing crystal formation and driving the system to reduce Gibbs energy by segregating into immiscible glassy phases (Hamann et al., 2018).

In contrast, in some terrestrial volcanic samples, extremely fast cooling (>1000 $K{\cdot}s^{-1}$) prevents phase separation, promoting homogenous glass formation. A cooling rate within 1–1000 $K{\cdot}s^{-1}$, however, facilitates the formation of intercrossed immiscible textures and skeletal mineral crystallites (Thivet et al., 2023). This principle applies to the immiscible conjugated liquid pairs and ilmenite crystallites reported here in CE-5 lunar sample. Given the exposed degassing pits on the grain's surface, these phase-separated structures likely formed in the grain's interior, where the cooling rate was not too high, due to limited direct contacts with other lunar grains and heat radiation into the vacuum. Consequently, such textures are rarely found on the surface of impact-derived particles like impact glass or agglutinates.

Phase separation in impact glass influences element redistribution. Our findings (Tables S1 and S2 in Supporting Information S1) indicate that not all volatile elements are enriched in the Si-rich phase. For example, Na and K are concentrated in Si-rich phase, while P is more abundant in Fe-rich phase. Additionally, partition coefficients for K, Ca and Fe vary obviously between the conjugation liquid pairs of Fe-Glass-1/2 and K-Si-Glass and nanodroplets and K-Si-Glass (Table S2 in Supporting Information S1). This indicates that local physical and chemical conditions, such as temperature and compositional heterogeneity, affect element redistribution during the metastable unmixing.

Previous studies have shown that the CE-5 landing site experiences mild impact conditions dominated by low-velocity impacts (Zhao et al., 2023). Impact glass species, especially glass particles or fibers generated from impact ejection and surface amorphous rims, have been widely discussed (Y. Wu et al., 2023; Zellner, 2019; Zhao et al., 2023). The relatively lower energy input from micrometeoroids at mid–high latitudes promotes local melting, fragmentation, and reheating of phase-separated glass, leading to ripening of clusters and nanodroplets, element redistribution and formation of unusual silicate mineral crystals. Due to the difference in viscosity changes upon heating, Fe-rich glass melts at lower temperatures than Si-rich glass. Consequently, small crystallites of uncommon silicates, such as those in Fe-Glass or Fe-rich nanodroplets reported here, would form more readily in these Fe-rich phases.

21699100, 2025, 7, Downloaded from https://agupubs.onlinelibrary.wiley.com/doi/10.1029/2025JE009028 by Sergio Sancevero - Capes , Wiley Online Library on [06/06/2026]. See the Terms and Conditions (https://onlinelibrary.wiley.com/terms-and-conditions) on Wiley Online Library for rules of use; OA articles are governed by the applicable Creative Commons License

5. Conclusion

In this study, we present for the first time, an integrated analysis of phase-separated glassy structure in a lunar soil grain classified as a new type of "impact glass." We describe the delicate morphologies of interfaces and ripening textures of chemically conjugated silicate nanodroplets at the nanoscale. We attribute their formation to the metastable immiscibility driven by chemical heterogeneities and rapid quenching. These findings significantly advance our understanding of impact-related evolution and behavior of lunar surface materials, providing valuable structural constraints for further research into lunar impact history and volatile distribution.

Data Availability Statement

The SEM images of the researched CE-5 lunar regolith grain and the TEM and STEM images of the structures containing silicate nanodroplets used in this manuscript are available at Science Data Bank (Dai et al., 2025, https://doi.org/10.57760/sciencedb.21150). The quasi-ternary phase plots were made with python-ternary version 1.0.6 (Harper et al., 2019). The crystal structures and SAED images were analyzed by ReciPro (Seto & Ohtsuka, 2022).

Acknowledgments
The lunar sample used in this study was provided by the China National Space Administration. This work was supported by Beijing Natural Science Foundation (Grant F251007); National Natural Science Foundation of China, Grants 22172003 and 92477203; the CAS Interdisciplinary Innovation Team, Grant JCTD-2020-18. We thank the Nanjing Institute of Geology and Palaeontology, Chinese Academy of Sciences for the use of the FIB-SEM. We thank the Electron Microscopy Laboratory and the Analytical Instrumentation Center at Peking University for the use of the aberration-correction electron microscopes. We thank the High-performance Computing Platform of Peking University for using computation resources.

References

Bennett, C. J., Pirim, C., & Orlando, T. M. (2013). Space-weathering of solar system bodies: A laboratory perspective. *Chemical Reviews*, *113*(12), 9086–9150. https://doi.org/10.1021/cr400153k

Blewett, D. T., Denevi, B. W., Cahill, J. T. S., & Klima, R. L. (2021). Near-UV and near-IR reflectance studies of lunar swirls: Implications for nanosize iron content and the nature of anomalous space weathering. *Icarus*, *364*, 114472. https://doi.org/10.1016/j.icarus.2021.114472

Bruno, M., Cremonese, G., & Marchi, S. (2007). Neutral sodium atoms release from the surfaces of the Moon and Mercury induced by meteoroid impacts. *Planetary and Space Science*, *55*(11), 1494–1501. https://doi.org/10.1016/j.pss.2006.10.006

Cassidy, W., & Hapke, B. (1975). Effects of darkening processes on surfaces of airless bodies. *Icarus*, *25*(3), 371–383. https://doi.org/10.1016/0019-1035(75)90002-0

Charlier, B., Namur, O., & Grove, T. L. (2013). Compositional and kinetic controls on liquid immiscibility in ferrobasalt–rhyolite volcanic and plutonic series. *Geochimica et Cosmochimica Acta*, *113*, 79–93. https://doi.org/10.1016/j.gca.2013.03.017

Chen, Y., Hu, S., Li, J. H., Li, Q. L., Li, X., Li, Y., et al. (2023). Chang'e-5 lunar samples shed new light on the Moon. *The Innovation Geoscience*, *1*(1), 100014. https://doi.org/10.59717/j.xinn-geo.2023.100014

Christoffersen, R., McKay, D. S., & Keller, L. P. (1996). Microstructure, chemistry, and origin of grain rims on ilmenite from the lunar soil finest fraction. *Meteoritics & Planetary Sciences*, *31*(6), 835–848. https://doi.org/10.1111/j.1945-5100.1996.tb02117.x

Cintala, M. J. (1992). Impact-induced thermal effects in the lunar and Mercurian regoliths. *Journal of Geophysical Research*, *97*(E1), 947–973. https://doi.org/10.1029/91JE02207

Cymes, B. A., Burgess, K. D., & Stroud, R. M. (2022). Detection of ferric iron in an exsolved lunar pyroxene using electron energy loss spectroscopy (EELS): Implications for space weathering and redox conditions on the Moon. *Meteoritics & Planetary Sciences*, *58*(2), 259–274. https://doi.org/10.1111/maps.13941

Dai, Y. H., Xie, Z. H., Li, Z. Z., Jia, T. Y., Wang, R. M., Yin, Z. J., et al. (2025). Raw image files of conjugated silicate nanodroplets found in CE-5 lunar regolith sample (Version 1) [Dataset]. *Science Data Bank*. https://doi.org/10.57760/sciencedb.21150

Freestone, I. C. (1978). Liquid immiscibility in alkali-rich magmas. *Chemical Geology*, *23*(1–4), 115–123. https://doi.org/10.1016/0009-2541(78)90069-4

Hamann, C., Fazio, A., Ebert, M., Hecht, L., Wirth, R., Folco, L., et al. (2018). Silicate liquid immiscibility in impact melts. *Meteoritics & Planetary Sciences*, *53*(8), 1594–1632. https://doi.org/10.1111/maps.12907

Harper, M., Weinstein, B., Simon, C., Morgan, W., Knight, V., Swanson, N., et al. (2019). marcharper/python-ternary: Version 1.0.6 [Software]. *Zenodo*. https://doi.org/10.5281/zenodo.594435

Harries, D., & Langenhorst, F. (2013). The nanoscale mineralogy of Fe,Ni sulfides in pristine and metamorphosed CM and CM/CI-like chondrites: Tapping a petrogenetic record. *Meteoritics & Planetary Sciences*, *48*(5), 879–903. https://doi.org/10.1111/maps.12089

Heiken, G. (1975). Petrology of lunar soils. *Reviews of Geophysics*, *13*(4), 567–587. https://doi.org/10.1029/RG013i004p00567

Heiken, G., Vaniman, D., & French, B. M. (Eds.) (1991)., *Lunar sourcebook: A user's guide to the moon*. Cambridge University Press.

Keller, L. P., Berger, E. L., Zhang, S., & Christoffersen, R. (2021). Solar energetic particle tracks in lunar samples: A transmission electron microscope calibration and implications for lunar space weathering. *Meteoritics & Planetary Sciences*, *56*(9), 1685–1707. https://doi.org/10.1111/maps.13732

Keller, L. P., & McKay, D. S. (1993). Discovery of vapor deposits in the lunar regolith. *Science*, *261*(5126), 1305–1307. https://doi.org/10.1126/science.261.5126.1305

Keller, L. P., & McKay, D. S. (1997). The nature and origin of rims on lunar soil grains. *Geochimica et Cosmochimica Acta*, *61*(11), 2331–2341. https://doi.org/10.1016/S0016-7037(97)00085-9

Li, C., Guo, Z., Li, Y., Tai, K., Wei, K., Li, X., et al. (2022). Impact-driven disproportionation origin of nanophase iron particles in Chang'e-5 lunar soil sample. *Nature Astronomy*, *6*(10), 1156–1162. https://doi.org/10.1038/s41550-022-01763-3

Li, C. L., Hu, H., Yang, M. F., Pei, Z. Y., Zhou, Q., Ren, X., et al. (2022). Characteristics of the lunar samples returned by the Chang'E-5 mission. *National Science Review*, *9*(2), nwab188. https://doi.org/10.1093/nsr/nwab188

Li, L., Hui, H., Hu, S., Wang, H., Yang, W., Chen, Y., et al. (2023). Petrogenesis of Chang'E-5 young mare low-Ti basalts. *Meteoritics & Planetary Sciences*, *58*(10), 1429–1448. https://doi.org/10.1111/maps.14071

Matsumoto, T., Harries, D., Langenhorst, F., Miyake, A., & Noguchi, T. (2020). Iron whiskers on asteroid Itokawa indicate sulfide destruction by space weathering. *Nature Communications*, *11*(1), 1117. https://doi.org/10.1038/s41467-020-14758-3

21699100, 2025, 7, Downloaded from https://agupubs.onlinelibrary.wiley.com/doi/10.1029/2025JE009028 by Sergio Sancevero - Capes , Wiley Online Library on [06/06/2026]. See the Terms and Conditions (https://onlinelibrary.wiley.com/terms-and-conditions) on Wiley Online Library for rules of use; OA articles are governed by the applicable Creative Commons License

Miyahara, M., El Goresy, A., Ohtani, E., Nagase, T., Nishijima, M., Vashaei, Z., et al. (2008). Evidence for fractional crystallization of wadsleyite and ringwoodite from olivine melts in chondrules entrained in shock-melt veins. *Proceedings of the National Academy of Sciences*, *105*(25), 8542–8547. https://doi.org/10.1073/pnas.0801518105

Mysen, B. O., & Cody, G. D. (2001). Silicate-phosphate interactions in silicate glasses and melts: II. Quantitative, high-temperature structure of P-bearing alkali aluminosilicate melts. *Geochimica et Cosmochimica Acta*, *65*(14), 2413–2431. https://doi.org/10.1016/S0016-7037(01)00598-1

Noble, S. K., Pieters, C. M., & Keller, L. P. (2007). An experimental approach to understanding the optical effects of space weathering. *Icarus*, *192*(2), 629–642. https://doi.org/10.1016/j.icarus.2007.07.021

Phinney, W. C., Warner, J. L., & Simonds, C. H. (1974). *Lunar highland rock types: Their implications for impact-induced fractionation* (Vol. 1, pp. 91–126). National Aeronautics and Space Administration.

Pieters, C. M., & Noble, S. K. (2016). Space weathering on airless bodies. *Journal of Geophysical Research: Planets*, *121*(10), 1865–1884. https://doi.org/10.1002/2016JE005128

Rode, O. D., Ivanov, A. V., Nazarov, M. A., Cimbálníková, A., & Jurek, K. (1980). *Atlas of photomicrographs of the surface structures of lunar regolith particles* (Vol. 1). Springer. Retrieved from https://linkinghub.elsevier.com/retrieve/pii/0019103580902559

Roedder, E. (1978). Silicate liquid immiscibility in magmas and in the system K_2O-FeO-Al_2O_3-SiO_2: An example of serendipity. *Geochimica et Cosmochimica Acta*, *42*(11), 1597–1617. https://doi.org/10.1016/0016-7037(78)90250-8

Roedder, E., & Weiblen, P. W. (1970). Lunar petrology of silicate melt inclusions, Apollo 11 rocks. *Proceedings of the Apollo 11 Lunar Science Conference*, *1*, 801–837. Paper presented at the Proceedings of the Apollo 11 Lunar Science Conference.

Roedder, E., & Weiblen, P. W. (1971). Petrology of silicate melt inclusions, Apollo 11 and Apollo 12 and terrestrial equivalents. *Paper presented at the Proceedings of the Second Lunar Science Conference, Proceedings of the Second Lunar Science Conference*, *1*, 507–528.

Rubin, A. E., Sailer, A. L., & Wasson, J. T. (1999). Troilite in the chondrules of type-3 ordinary chondrites: Implications for chondrule formation. *Geochimica et Cosmochimica Acta*, *63*(15), 2281–2298. https://doi.org/10.1016/S0016-7037(99)00119-2

Sensarma, S., & Palme, H. (2013). Silicate liquid immiscibility in the ∼ 2.5 Ga Fe-rich andesite at the top of the Dongargarh large igneous province (India). *Lithos*, *170–171*, 239–251. https://doi.org/10.1016/j.lithos.2013.03.004

Seto, Y., & Ohtsuka, M. (2022). ReciPro: Free and open-source multipurpose crystallographic software integrating a crystal model database and viewer, diffraction and microscopy simulators, and diffraction data analysis tools [Software]. *Journal of Applied Crystallography*, *55*(2), 397–410. https://doi.org/10.1107/S1600576722000139

Stern, S. A. (1999). The lunar atmosphere: History, status, current problems, and context. *Reviews of Geophysics*, *37*(4), 453–491. https://doi.org/10.1029/1999RG900005

Thivet, S., Pereira, L., Menguy, N., Médard, É., Verdurme, P., Berthod, C., et al. (2023). Metastable liquid immiscibility in the 2018–2021 Fani Maoré lavas as a mechanism for volcanic nanolite formation. *Communications Earth and Environment*, *4*(1), 483. https://doi.org/10.1038/s43247-023-01158-w

Thompson, A. B., Aerts, M., & Hack, A. C. (2007). Liquid immiscibility in silicate melts and related systems. *Reviews in Mineralogy and Geochemistry*, *65*(1), 99–127. https://doi.org/10.2138/rmg.2007.65.4

Toulmin, P., & Barton, P. B. (1964). A thermodynamic study of pyrite and pyrrhotite. *Geochimica et Cosmochimica Acta*, *28*(5), 641–671. https://doi.org/10.1016/0016-7037(64)90083-3

Veksler, I. V., Dorfman, A. M., Danyushevsky, L. V., Jakobsen, J. K., & Dingwell, D. B. (2006). Immiscible silicate liquid partition coefficients: Implications for crystal-melt element partitioning and basalt petrogenesis. *Contributions to Mineralogy and Petrology*, *152*(6), 685–702. https://doi.org/10.1007/s00410-006-0127-y

Veksler, I. V., Dorfman, A. M., Rhede, D., Wirth, R., Borisov, A. A., & Dingwell, D. B. (2008). Liquid unmixing kinetics and the extent of immiscibility in the system K_2O–CaO–FeO–Al_2O_3–SiO_2. *Chemical Geology*, *256*(3–4), 119–130. https://doi.org/10.1016/j.chemgeo.2008.06.033

Visser, W., & Koster Van Groos, A. F. (1979). Phase relations in the system K_2O-FeO-Al_2O_3-SiO_2 at 1 atmosphere with special emphasis on low temperature liquid immiscibility. *American Journal of Science*, *279*(1), 70–91. https://doi.org/10.2475/ajs.279.1.70

Wu, F. Y., Li, Q. L., Chen, Y., Hu, S., Yue, Z. Y., Zhou, Q., et al. (2024). Lunar evolution in light of the Chang'e-5 returned samples. *Annual Review of Earth and Planetary Sciences*, *52*(1), 6–194. https://doi.org/10.1146/annurev-earth-040722-100453

Wu, Y., Liao, S., Yan, P., Xiao, Z., Yin, Z., Yang, W., et al. (2023). Impact-related chemical modifications of the Chang'E-5 lunar regolith. *Geochimica et Cosmochimica Acta*, *363*, 94–113. https://doi.org/10.1016/j.gca.2023.10.031

Xian, H., Zhu, J., Yang, Y., Li, S., Lin, X., Xi, J., et al. (2023). Ubiquitous and progressively increasing ferric iron content on the lunar surfaces revealed by the Chang'e-5 sample. *Nature Astronomy*, *7*(3), 280–286. https://doi.org/10.1038/s41550-022-01855-0

Yan, P., Xiao, Z., Wu, Y., Wu, Y., Pan, Q., Luo, F., & Xu, R. (2024). Submicroscopic iron-rich grains throughout impact glasses in Chang'E-5 regolith. *Icarus*, *410*, 115920. https://doi.org/10.1016/j.icarus.2023.115920

Yan, P., Xiao, Z., Wu, Y., Yang, W., Li, J., Gu, L., et al. (2022). Intricate regolith reworking processes revealed by microstructures on lunar impact glasses. *Journal of Geophysical Research: Planets*, *127*(12), e2022JE007260. https://doi.org/10.1029/2022JE007260

Yang, J., & Du, W. (2024). High-pressure minerals and new lunar mineral changesite-(Y) in Chang'e-5 regolith. *Matter and Radiation at Extremes*, *9*(2), 027401. https://doi.org/10.1063/5.0148784

Zellner, N. E. B. (2019). Lunar impact glasses: Probing the Moon's surface and constraining its impact history. *Journal of Geophysical Research: Planets*, *124*(11), 2686–2702. https://doi.org/10.1029/2019je006050

Zhao, R., Shen, L., Xiao, D., Chang, C., Huang, Y., Yu, J., et al. (2023). Diverse glasses revealed from Chang'E-5 lunar regolith. *National Science Review*, *10*(12), nwad079. https://doi.org/10.1093/nsr/nwad079

21699100, 2025, 7, Downloaded from https://agupubs.onlinelibrary.wiley.com/doi/10.1029/2025JE009028 by Sergio Sancevero - Capes , Wiley Online Library on [06/06/2026]. See the Terms and Conditions (https://onlinelibrary.wiley.com/terms-and-conditions) on Wiley Online Library for rules of use; OA articles are governed by the applicable Creative Commons License